Zhang, Jin, Muiña, Alejandra Traspas, Mifsud, Duncan V, Kaňuchová, Zuzana, Cielinska, Klaudia, Herczku, Péter, Rahul, K K, Kovács, Sándor T S, Rácz, Richárd, Santos, Julia C and others (2024) *A systematic IR and VUV spectroscopic investigation of ion, electron, and thermally processed ethanolamine ice.* Monthly Notices of the Royal Astronomical Society . ISSN 1365-2966.

A systematic IR and VUV spectroscopic investigation of ion, electron, and thermally processed ethanolamine ice

Jin Zhang [1]*† Alejandra Traspas Muiña [1,2]*† Duncan V. Mifsud,[3] Zuzana Kaňuchová,[4]
Klaudia Cielinska,[5] Péter Herczku,[3] K. K. Rahul,[3] Sándor T. S. Kovács,[3] Richárd Rácz,[3] Julia
C. Santos [6] Alfred T. Hopkinson,[7] Luca Craciunescu [8] Nykola C. Jones,[9] Søren V. Hoffmann,[9]
Sándor Biri,[3] István Vajda,[3] István Rajta,[3] Anita Dawes,[10] Bhalamurugan Sivaraman,[11] Zoltán Juhász,[3]
Béla Sulik,[3] Harold Linnartz,[6]‡ Liv Hornekær,[7] Felipe Fantuzzi [12] Nigel J. Mason[3,5]
and Sergio Ioppolo[1,7]*

Affiliations are listed at the end of the paper

ABSTRACT

The recent detection of ethanolamine (EtA, $HOCH_2CH_2NH_2$), a key component of phospholipids, i.e. the building blocks of cell membranes, in the interstellar medium is in line with an exogenous origin of life-relevant molecules. However, the stability and survivability of EtA molecules under inter/circumstellar and Solar System conditions have yet to be demonstrated. Starting from the assumption that EtA mainly forms on interstellar ice grains, we have systematically exposed EtA, pure and mixed with amorphous water (H_2O) ice, to electron, ion, and thermal processing, representing 'energetic' mechanisms that are known to induce physicochemical changes within the ice material under controlled laboratory conditions. Using infrared (IR) spectroscopy, we have found that heating of pure EtA ice causes a phase change from amorphous to crystalline at 180 K, and further temperature increase of the ice results in sublimation-induced losses until full desorption occurs at about 225 K. IR and vacuum ultraviolet (VUV) spectra of EtA-containing ices deposited and irradiated at 20 K with 1 keV electrons as well as IR spectra of H_2O:EtA mixed ice obtained after 1 MeV He^+ ion irradiation have been collected at different doses. The main radiolysis products, including H_2O, CO, CO_2, NH_3, and CH_3OH, have been identified and their formation pathways are discussed. The measured column density of EtA is demonstrated to undergo exponential decay upon electron and ion bombardment. The half-life doses for electron and He^+ ion irradiation of pure EtA and H_2O:EtA mixed ice are derived to range between 10.8–26.3 eV/16u. Extrapolating these results to space conditions, we conclude that EtA mixed in H_2O ice is more stable than in pure form and it should survive throughout the star and planet formation process.

Key words: astrochemistry – radiation: dynamics – methods: laboratory: molecular – techniques: spectroscopic – infrared: ISM – ultraviolet: ISM.

1 INTRODUCTION

The theory of an extra-terrestrial origin for many of the complex organic molecules (COMs) thought to be key to the emergence of life on Earth is supported by the discovery of more than 300 individual species in the interstellar medium (ISM) (McGuire 2022), as well as the detection of various biomolecules such as proteinogenic amino acids in comets and asteroids (Glavin, Dworkin & Sandford 2008; Altwegg et al. 2016). One class of biomolecule that has received increasing attention from the astronomical and astrochemical communities is that of phospholipids, the building blocks of cellular membranes.

Indeed, indirect evidence of their extra-terrestrial origin has appeared in the form of the detection of their structural sub-components (e.g. fatty acids, alcohols, and phosphonic acids) in meteorites (Cooper, Onwo & Cronin 1992; Sephton 2002; Pizzarello & Shock 2010). Laboratory experiments have also successfully synthesized glycerol phosphates, precursor molecules for lipid biosynthesis, in interstellar ice analogues subjected to space conditions (Zhu et al. 2020).

The recent detection of the simplest phospholipid hydrophilic head-group, ethanolamine (EtA; IUPAC name: 2-aminoethanol; formula: $HOCH_2CH_2NH_2$ or C_2H_7NO), in interstellar space (Rivilla et al. 2021), combined with its previously known existence within the Almahata Sitta meteorite (Glavin et al. 2010), further strengthens the possibility of an exogenous origin for life's biomolecules. Interestingly, the work by Rivilla et al. (2021) suggests that EtA in the ISM could be seeded to planetesimals during the formation of the Solar System and subsequently transferred to the early Earth. Such an idea is not unreasonable, particularly in light of the fact that many

Table 1. Summary of the experiments on EtA ices performed as part of our systematic study. Note that, the mass densities of the pure EtA ices were assumed to be 1.01 g cm^{-3} (Reitmeier, Sivertz & Tartar 1940), while those of the H$_2$O:EtA mixed ices were approximated by that of ASW which has been reported to be 0.94 g cm^{-3} (Ghormley & Hochanadel 1971).

Ice Sample	1[†]	2	3	4	5	6
Composition	Pure EtA	Pure EtA	Pure EtA	H$_2$O:EtA (50:1)	H$_2$O:EtA (20:1)	H$_2$O:EtA (50:1)
Temperature (K)	20-225	20	20	20	20	20
Thickness (μm)	0.33	0.34	0.04	1.90	0.03	1.40
Projectile	–	1 keV e$^-$	1 keV e$^-$	1 keV e$^-$	1 keV e$^-$	1 MeV He$^+$
Penetration depth (μm)	–	0.045	0.045	0.050	0.050	5.6
Stopping power (eV Å^{-1})	–	2.22	1.98	2.00	2.00	25.13
Mass stopping power ($\times 10^{-15}$ eV cm^2/16u)	–	5.88	5.23	5.69	5.69	71.40
Spectroscopic analysis	IR	IR	VUV	IR	VUV	IR
Facility	Atomki	Atomki	ASTRID2	Atomki	ASTRID2	Atomki

Note. [†] Non-irradiative heating experiment.

prebiotic molecules and biomolecules accreting in circumstellar dust are thought to be able to survive the many meteoritic and cometary collisions that characterized the surface of the early Earth (Bertrand et al. 2009; McCaffrey et al. 2014). Once delivered to the primitive Earth, EtA could, in principle, participate in the synthesis of phospholipids (Oró et al. 1978; Rao, Eichberg & Oró 1987), which may then go on to form primitive cell membranes within which proto-metabolisms may arise (Budin & Szostak 2011; Monnard & Deamer 2011).

The efficient synthesis and stability of EtA under astrophysical conditions are essential pre-requisites for its successful delivery to the early Earth and any possible resultant phospholipid formation. Therefore, it is highly desirable to identify the formation routes and the stability of EtA within the ISM. Thus far, the chemical mechanisms by which interstellar EtA may form remain unclear, although several possibilities are summarized by Rivilla et al. (2021), including: (i) the grain-catalysed hydrogenation of HNCCO (Ehrenfreund & Charnley 2001), (ii) the barrierless reactions between either NH$_3$+C + CO or NH$_2$ + CH + CO to form NH$_2$CHCO (Suzuki et al. 2018; Krasnokutski 2021) followed by further hydrogenation to yield EtA, (iii) the reaction between CO and NH$_2$CH$_2$ to yield NH$_2$CH$_2$CO (Suzuki et al. 2018) followed by further hydrogenation to form EtA, (iv) non-diffusive chemistry between NH$_2$CH$_2$ + CH$_2$OH on the surfaces of dust grains (Fedoseev et al. 2015b; Ioppolo et al. 2021a), and (v) the reaction from ethylene, C$_2$H$_4$ + OH → C$_2$H$_4$OH, followed by the radical–radical reaction C$_2$H$_4$OH + NH$_2$ → NH$_2$CH$_2$CH$_2$OH (Molpeceres & Rivilla 2022). Additionally, recent studies have shown that the carbon atom C(^{3}P) is reactive with components of interstellar ice, such as H$_2$O (Potapov et al. 2021; Molpeceres et al. 2021) and CO (Fedoseev et al. 2022; Ferrero et al. 2023), and a possible product formed as a result of this chemistry, :C = C = O, could be a building block for EtA molecules. Unfortunately, none of the aforementioned larger precursors has been unambiguously detected in the ISM due either to a lack of laboratory-generated rotational spectra or their possible rapid consumption in these reactions, and so the interstellar chemistry leading to the formation of EtA remains shrouded in mystery for now.

In this paper, we detail the results of a series of experiments conducted to assess the radiation stability of EtA ice when impinged upon by a 1 keV electron beam as well as a 1 MeV He$^+$ ion beam, simulating a variety of interstellar-relevant ionizing radiation processes. In order to monitor radiation-induced chemical changes within the ice, we have made extensive use of *in situ* infrared (IR) and vacuum-ultraviolet (VUV) absorption spectroscopy. Furthermore, we have also collected spectra of the pristine (i.e. unirradiated) EtA

ice at various temperatures so as to aid in the interpretation of our spectroscopic results. The results are further supported by density functional theory (DFT), time-dependent density functional theory (TDDFT), and the domain-based local pair natural orbital (DLPNO; Riplinger & Neese 2013; Riplinger et al. 2013) implementation of similarity transformed equation-of-motion coupled-cluster theory (STEOM-CCSD; Nooijen & Bartlett 1997), collectively referred to as DLPNO-STEOM-CCSD. Our IR and VUV spectroscopic characterizations and our electron and He$^+$ ion irradiations constitute an important step towards a better understanding of the synthesis and evolution of primitive cell membranes. The IR data will further aid the interpretation of observational results from the JWST, while the VUV data will support spectroscopic data collected by interplanetary missions such as the *Jupiter Icy Moons Explorer* (*JUICE*).

2 EXPERIMENTAL METHODOLOGY

Electron and He$^+$ ion irradiation experiments of EtA, both pure and mixed with amorphous solid water (ASW), along with heating experiments of pure EtA ice, were conducted to simulate the different types of processing to which EtA ices may be subjected in different astronomical environments. The first series of measurements was performed at the HUN–REN Institute for Nuclear Research (Atomki) in Debrecen, Hungary, where ices were processed by electron and He$^+$ ion irradiation as well as thermal annealing, and physico-chemical changes in the ice were quantitatively monitored using IR spectroscopy. The second series of measurements took place at the AU–UV beam line of the ASTRID2 synchrotron light source at Aarhus University, Denmark, where ices were processed by electron irradiation and investigated using VUV spectroscopy. The remainder of this section is devoted to a description of the experimental set-ups and techniques used throughout this study, as well as of the computational calculations performed to support the interpretation of the laboratory work. A summary of the experiments performed is provided in Table 1.

2.1 IR spectroscopy at Atomki

Experiments performed at Atomki were carried out using the Ice Chamber for Astrophysics–Astrochemistry (ICA). This experimental set-up has been described in detail in previous publications (Herczku et al. 2021; Mifsud et al. 2021), and hence only a brief overview is provided here. The ICA is an ultrahigh vacuum (UHV)-compatible chamber with a base pressure of 10^{-9} mbar, which is maintained through the combined action of a rough dry vacuum pump and a

turbomolecular pump. Within the centre of the chamber is a gold-coated, oxygen-free high conductivity (OFHC) copper sample holder hosting a series of ZnSe deposition substrates (see fig. 3 in Herczku et al. 2021) onto which astrophysical ice analogues may be prepared. The sample holder and deposition substrates can be cooled to 20 K by a closed-cycle helium cryostat.

A Thermo Nicolet Nexus 670 Fourier-transform mid-infrared (FTIR) spectrophotometer having a spectral range of 4000–650 cm^{-1} (2.5–15.4 μm) and a nominal resolution of 0.5 cm^{-1} was used to quantitatively monitor physicochemical changes in our EtA-containing ices induced by thermal or radiolytic processing. In the present setup (see fig. 4 in Herczku et al. 2021), the transmitted IR beam is detected by using a mercury–cadmium–telluride (MCT) detector placed outside the main vacuum chamber in a small external container. A purge box continuously passes purified air through this MCT detector chamber as well as the entire IR pathway so as to prevent absorption by air constituents of variable composition (e.g. H_2O or CO_2). IR spectra were acquired as collections of 256 co-added scans.

2.1.1 Heating experiments

EtA purchased from Merck (>99.5 per cent purity, CAS 141-43-5) was first degassed in a glass vial using the standard liquid nitrogen freeze-pump-thaw technique. It was subsequently dosed into the main chamber and directly deposited onto the ZnSe substrates at 20 K *via* a custom-built direct dosing line. After deposition of the ice, an IR absorption spectrum was collected, and the ice was subsequently warmed at a rate of 2 K min^{-1} with additional spectra collected at 10 K intervals until total sublimation of the ice occurred at 225 K.

The column density N (molecules cm^{-2}) and thickness d (μm) of a deposited interstellar ice analogue studied using IR spectroscopy was calculated through the following equations:

$$N = \frac{\ln(10) \times \int A(\nu)\, d\nu}{A}, \tag{1}$$

$$d = 10^4 \times \frac{Nm}{N_A \rho}, \tag{2}$$

where $A(\nu)$ is the wavenumber-dependent absorbance of a characteristic IR absorption band, A is the integrated strength constant of that band, m is the molecular mass of the molecule, N_A is the Avogadro constant, and ρ is the ice density. As there are no available literature values on the density of pure EtA ice at 20 K, we have made use of a density value of 1.01 g cm^{-3}, which represents the mass density of EtA under standard temperature and pressure conditions (Reitmeier et al. 1940). In the case of EtA mixed with ASW with ratios of 50:1 and 20:1 in favour of H_2O, the ASW density value of 0.94 g cm^{-3} was used to calculate the thickness of the ice (Ghormley & Hochanadel 1971). Since our study is the first to consider the IR spectroscopy of an EtA interstellar ice analogue, we cannot make use of previous literature values of the integrated strength constants of its absorption bands. As such, we have followed the procedure previously published in Fuchs et al. (2009) that uses isothermal desorption experiments to estimate the band strength of a molecule as described in section 3.1.2.

2.1.2 1 keV electron irradiation experiments

Electron irradiation experiments were conducted by means of a Kimball ELG-2A electron gun that is affixed to the side wall of the ICA. This gun is able to emit stable, mono-energetic electron beams having kinetic energies between 5–2000 eV. Prior to irradiation, the

beam current, stability, and profile of the 1 keV electron beam used for this study were determined using the method described by Mifsud et al. (2021).

A pure EtA ice and an H_2O:EtA (50:1) mixed ice were each deposited at 20 K, after which an IR absorption spectrum of each ice was acquired. The ices were subsequently irradiated using 1 keV electrons, with incident electrons impacting the ice at an angle of 36° to the normal at a flux of 3.2×10^{13} electrons s^{-1} cm^{-2}. The ices were irradiated for a total of 1 h, corresponding to a delivered fluence of 1.2×10^{17} electrons cm^{-2}. Additional IR spectra were acquired at pre-defined fluence intervals.

2.1.3 1 MeV He^+ ion irradiation experiments

The ion irradiation of an H_2O:EtA (50:1) mixed ice was also performed. Similarly to the electron irradiation experiments, an IR absorption spectrum was acquired directly after deposition of the ice. The mixed ice was then irradiated with a 1 MeV He^+ ion beam delivered by a 2 MV Tandetron particle accelerator (Rajta et al. 2018; Biri et al. 2021), with ions being delivered to the ice at an angle of 36° to the normal and at a flux of 7.2×10^{11} He^+ ions s^{-1} cm^{-2} for 1 hour, corresponding to a total delivered fluence of 2.6×10^{15} He^+ ions cm^{-2}. Additional IR spectra were recorded at pre-defined fluence intervals.

2.2 VUV spectroscopy at ASTRID2

Experiments performed at the ASTRID2 synchrotron facility made use of the Portable Astrochemistry Chamber (PAC). This chamber has been described previously (Ioppolo et al. 2020, 2021b), and so we limit ourselves to a brief description of its most salient features. The PAC is a UHV-compatible spheroidal-cube chamber operating at a base pressure of 10^{-9} mbar. The chamber contains a rotatable OFHC copper sample holder hosting a MgF_2 substrate that can be cooled to 20 K by a closed-cycle helium cryostat. Interstellar ice analogues can be prepared *via* the deposition of dosed gases and vapours, which are first introduced into a pre-mixing line before being dosed into the main chamber through an all-metal leak valve for direct deposition.

The PAC is attached to the AU-UV beamline at the ASTRID2 synchrotron light source, which is able to produce monochromatic light over a wavelength range of 115–700 nm using two gratings (Eden et al. 2006; Palmer et al. 2015). The high-energy grating used for the experiments described in this paper has a typical flux of 10^{10} photons s^{-1} 100 mA^{-1} and a photon resolution of 0.08 nm. The step sizes for data collection in this work are 0.2 and 1 nm. A photomultiplier tube (PMT) mounted on the PAC chamber is used to measure the light produced by the AU–UV beam line being transmitted through the MgF_2 substrate and ices. It is important to note that the VUV radiation from ASTRID2 is used as a diagnostic tool to monitor chemical changes within the ices, rather than to photoprocess the ices. The VUV irradiation effects on the ices, i.e. photodesorption and photochemistry, are negligible due to the low VUV flux and low overall photon fluence used.

Similarly to the work at Atomki, EtA was purchased from Merck (>99.5 per cent purity) and was degassed using the standard liquid nitrogen freeze-pump-thaw technique before being used. Prior to deposition of the ice, the MgF_2 substrate was cooled to 20 K, then rapidly heated to 276 K so as to remove any contaminant species adsorbed on it, and then re-cooled to 20 K. The substrate was then rotated to face the inlet system of the dosing line, and a pure EtA ice or an H_2O:EtA (20:1) mixed ice were deposited in separate experiments.

The overall thickness of the deposited ice was determined by means of the He–Ne laser interference technique; more information on which can be found in the works of Goodman (1978) and Born & Wolf (2013). Briefly, this technique allows the thickness of the ice to be calculated as:

$$d = \frac{\lambda_0}{2n_1 \cos\theta} \times C, \qquad (3)$$

where λ_0 is the wavelength of the He–Ne laser beam *in vacuo* (632.8 nm), θ is the angle of the laser light within the ice, n_1 is the refractive index of the ice layer which is estimated from the ratio of the maxima and minima of the laser interference pattern, and C is the number of constructive pattern repetitions observed during the deposition of the ice.

It is to be noted that the deposition of an ice for a duration corresponding to a full interference fringe (i.e. $C = 1$, or one repetition in the laser interference pattern), oftentimes results in an ice which is sufficiently thick to cause saturation of its major VUV absorption features. In such cases, the deposition time corresponding to a full interference fringe was recorded and then the ice was subsequently heated from 20 K until sublimation. The known deposition time of one fringe and its corresponding ice thickness were then used to estimate a shorter deposition time so as to obtain a thinner ice having a spectrum with no saturated absorption features.

The electron irradiations of a pure EtA ice and an H_2O:EtA (20:1) mixed ice were examined in separate experiments. An ice was first deposited at 20 K, after which a VUV absorption spectrum was acquired. The ice was then irradiated using 1 keV electrons by means of a Kimball FRA-2X1-5549 electron gun, with incident electrons impacting orthogonal to the plane of the ice. The ice was irradiated using a flux of 2×10^{13} electrons s^{-1} cm^{-2} for 1 h, corresponding to an overall delivered fluence of 7.2×10^{16} electrons cm^{-2}. During each irradiation, additional VUV absorption spectra were acquired at pre-defined fluence intervals.

2.3 Computational details

Calculations were performed to simulate the IR and VUV spectra of EtA ice, aiding in the identification and interpretation of experimentally observed absorption bands. All DFT calculations were carried out using the GAUSSIAN 16, Revision C.01 quantum chemistry package (Frisch et al. 2016), while TDDFT and DLPNO-STEOM-CCSD computations were conducted with ORCA 5.0.4 (Neese 2022). Geometry optimizations were performed with the PBE0 functional (Adamo & Barone 1999; Ernzerhof & Scuseria 1999) and the def2-TZVP (Weigend & Ahlrichs 2005) basis set.Dispersion corrections were included in the optimizations using Grimme's D3 method (Grimme et al. 2010) combined with the Becke–Johnson (BJ) correction (Grimme, Ehrlich & Goerigk 2011). This level of theory is referred to as PBE0-D3(BJ)/def2-TZVP. We selected this DFT functional based on its proven performance for structural properties of various small to medium-sized organic molecules, as supported by distinct benchmark studies (e.g. Kozuch & Martin 2013; Brémond et al. 2016; Sharma & Champagne 2022). The calculations were performed for distinct conformers of the isolated EtA molecule and EtA clusters, considering stoichiometries of up to four molecules, (EtA)$_4$. These clusters were built from special cuts of the EtA crystal structure obtained by Romanini et al. (2019) and from selected structures taken from Vorobyov, Yappert & DuPré (2002). Indeed, cluster-based quantum chemical calculations employing DFT offer a robust approach for simulating and interpreting the vibrational (Chizallet et al. 2007; Yuan et al. 2018; Zhang et al.

2021; Kalout et al. 2022) and electronic (Craciunescu et al. 2023) properties of condensed-phase systems and molecular crystals. This is contingent upon the proper consideration of available crystal X-ray data and cluster symmetry (Katsyuba et al. 2020; Craciunescu et al. 2022). All optimized geometries are characterized as minima on the corresponding potential energy surfaces by vibrational frequency calculations, which revealed that all eigenvalues of the Hessian matrices are positive. A scaling factor of 0.96 was applied to all vibrational frequencies obtained in this study to account for approximations in electronic structure calculations and vibrational anharmonic effects. This value, which depends on the level of theory and basis set used, was chosen based on recommendations from the NIST Computational Chemistry Comparison and Benchmark Database (CCCBDB; Johnson 2022).

Vertical excitation energies considering up to 20 singlet states were computed for distinct conformers of EtA (see the Supplementary data for further information) utilizing the TDDFT approach in order to simulate their UV-vis spectra. These were done using the long-range corrected ωB97X-D3(BJ) hybrid functional (Chai & Head-Gordon 2008) and the quadruple-ζ def2-QZVPP basis set. A Lorentzian broadening with band width at half height of 10 nm was applied to all transitions. Additional electronic excitation calculations were performed at the DLPNO–STEOM–CCSD (Nooijen & Bartlett 1997; Riplinger & Neese 2013; Riplinger et al. 2013) level of theory and were used to validate the TDDFT results. For these, the quadruple-ζ def2-QZVPP basis set was also applied. The characterization of the electronic excitations was done by performing the natural transition orbital (NTO) analysis (Martin 2003). Inspired by recent studies in which accurate absorption spectra of organic semiconductor thin films were obtained by a cluster approach (Craciunescu et al. 2022, 2023), we extended our investigation to EtA oligomers. However, the differences between the vertical excitation energies of a single EtA molecule and its oligomers turned out to be negligible, so we limit the discussion of the calculated absorption spectrum to our results for the isolated molecule. All TDDFT electronic energies discussed herein are calculated at the ωB97X-D3(BJ)/def2-QZVPP//PBE0-D3(BJ)/def2-TZVP level of theory.

3 RESULTS AND DISCUSSION

3.1 Deposition and heating studies

3.1.1 Deposition of pure EtA ice

The IR spectrum of pure EtA ice with a thickness of 330 nm deposited at 20 K is displayed in Fig. 1. The absorption bands are listed in Table 2, and are assigned to corresponding vibrational modes according to published literature and our computational calculations. The intense peaks at around 3300 cm^{-1} are assigned to the NH$_2$ moiety; more precisely, to the symmetric and antisymmetric NH$_2$ fundamental stretching modes that are respectively identified at 3287 and 3353 cm^{-1} (Krueger & Mettee 1965; Silva et al. 1999; Knop, Lindner & Vöhringer 2011). Additionally, the OH fundamental stretching mode is located at 3187 cm^{-1}, and there are two CH stretching modes at 2857 and 2933 cm^{-1} (Knop et al. 2011). Compared to the gas-phase spectrum, these absorption bands show clear shifts to longer wavelengths, which is due to the formation of hydrogen bonds in the solid phase (Novak 1974; Kandratsenka, Schwarzer & Vöhringer 2008). This is also evident when comparing the computed IR peak of the OH stretching mode of the most stable gas-phase conformer of EtA (Radom et al. 1973; Silva et al. 1999) with that of the (EtA)$_2$-**I** dimer, which features an intermolecular
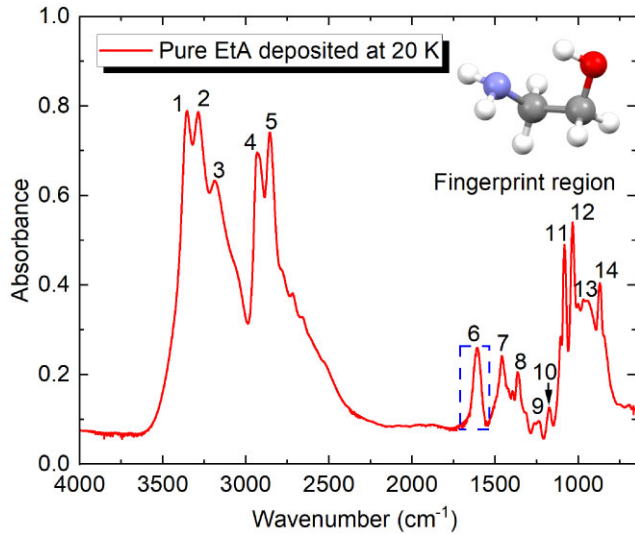
Figure 1. IR absorption spectrum of pure EtA ice after deposition at 20 K having a spectral resolution of $0.5\,\mathrm{cm}^{-1}$. The absorption band at $1615\,\mathrm{cm}^{-1}$ has been highlighted by a dashed blue rectangle. The 3D image of the global minimum structure of gas-phase EtA (Silva, Duarte & Fausto 1999) is also shown.

Table 2. Band assignments for the pure EtA ice deposited at 20 K.

Band No.	Wavenumber (cm^{-1})	Mode	References
1	3353	$\nu_{as}(NH_2)$	a, b, c
2	3287	$\nu_s(NH_2)$	a, b, c
3	3187	$\nu(OH)$	a
4	2933	$\nu_{as}(CH_2)$	a, c, d
5	2857	$\nu_s(CH_2)$	a, c, d
6	1615	$\delta(NH_2)$	c, d
7	1455	$\delta(CH_2)$	c, d
8	1365	$\omega(CH_2)$	c, d
9	1240	$\tau(CH_2)$	c, d
10	1178	$\rho(CH_2)$	c, d
11	1083	$\nu(C-O)$	c, d
12	1035	$\nu(C-N)$	c, d
13	968	$\omega(NH_2)$	c
14	870	$\nu(C-C)$	c

[a]Knop et al. (2011); [b]Krueger & Mettee (1965); [c]Silva et al. (1999); [d]Tseng et al. (2010).

OH$\cdots$NH$_2$ hydrogen bond (see top panel of Fig. 2). While the OH stretching mode of monomeric EtA is located at $3587\,\mathrm{cm}^{-1}$, the OH$\cdots$NH$_2$ stretching vibrational mode of the dimer $(EtA)_2$-**I** is found at $3351\,\mathrm{cm}^{-1}$, corresponding to a redshift of $236\,\mathrm{cm}^{-1}$. Similar redshifts are found for other $(EtA)_2$ isomers featuring OH$\cdots$NH$_2$ contacts, including the cyclic dimer $(EtA)_2$-**IV**, which was identified by Vorobyov et al. (2002) as the one featuring the highest OH$\cdots$NH$_2$ interaction energy. The computed IR absorption spectra for both the monomeric system as well as the various dimeric systems are displayed in the bottom panel of Fig. 2. The fingerprint region of the EtA spectrum shown in Fig. 1 contains a rather complicated series of absorption bands mainly due to bending vibrations within the molecule (Stuart 2004), for which the corresponding assignments are listed in Table 2. Among these bands, the band at $1615\,\mathrm{cm}^{-1}$ corresponding to the NH$_2$ bending mode is a relatively isolated one, as denoted by the blue rectangle therefore it will be used in

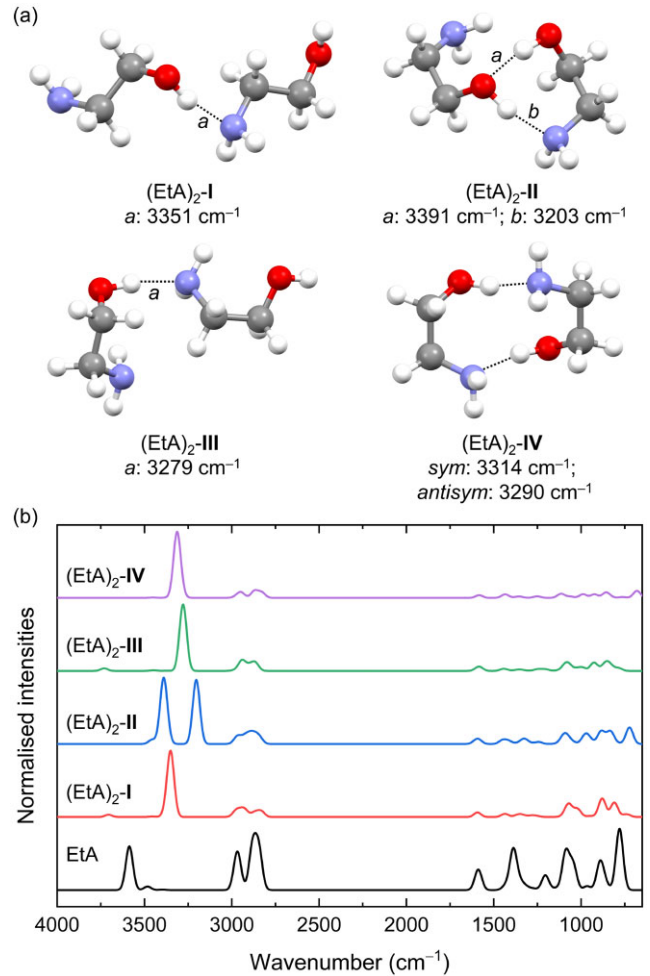**Figure 2.** (a) Molecular structure and computed OH$\cdots$X (X = NH$_2$, OH) vibrational frequencies of selected dimeric $(EtA)_2$ systems. (b) Simulated IR absorption spectra for EtA and different EtA dimeric systems. A scaling factor of 0.96 is applied to all calculated frequencies. In $(EtA)_2$-**II**, the two large peaks in the $3000-3500\,\mathrm{cm}^{-1}$ region correspond to the OH$\cdots$NH$_2$ $(3203\,\mathrm{cm}^{-1})$ and OH$\cdots$OH $(3391\,\mathrm{cm}^{-1})$ vibrations, respectively. In $(EtA)_2$-**IV**, the wavenumber values represent the positions of the symmetric (*sym*) and antisymmetric (*antisym*) OH$\cdots$NH$_2$ vibrations, which are coupled in this isomer. For comparison, the OH stretching of the most stable conformer of EtA in the gas phase is found at $3587\,\mathrm{cm}^{-1}$. Relative electronic energies corrected by zero-point energy (kcal mol^{-1}) are as follows: $(EtA)_2$-**I**: 7.4; $(EtA)_2$-**II**: 1.2; $(EtA)_2$-**III**: 3.9; $(EtA)_2$-**IV**: 0. All calculations were performed at the PBE0-D3(BJ)/def2-TZVP level of theory.

later subsections for the estimation of the integrated band strength constant and column density.

3.1.2 Heating of pure EtA ice

Two independent heating studies of pure EtA ices were carried out. The first was a gradual heating study over a temperature range of 20–225 K performed to determine the temperatures at which thermally induced phase changes and sublimation of the ice occurred, while the second study was a rapid heating experiment from 180 to 210 K followed by isothermal desorption so as to estimate the integrated band strength constant of a characteristic EtA absorption band, thus allowing for the deposited column density and thickness of the ice to be estimated.
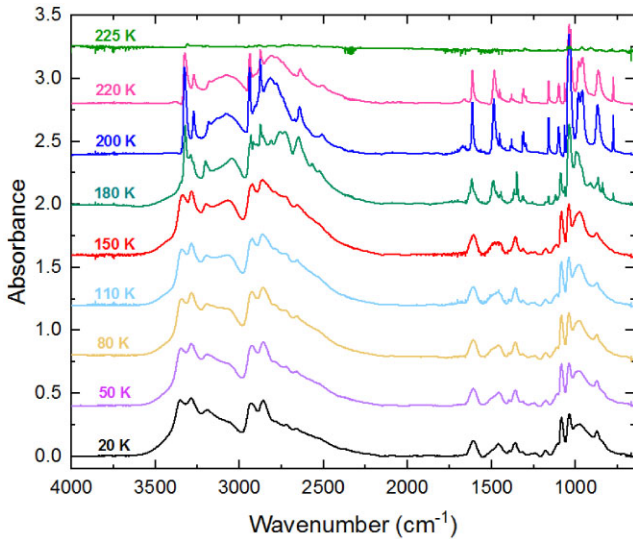
Figure 3. IR spectra of thermally annealed pure EtA ice acquired at temperatures ranging between 20–225 K. Spectra are vertically offset from one another for ease of viewing.

3.1.2.1 Phase change study A pure EtA ice deposited at 20 K was sequentially heated in an effort to understand the physicochemical changes occurring within the ice as a function of temperature. Once a post-deposition IR absorption spectrum was acquired, the ice was warmed to a temperature of 225 K at a rate of 2 K min^{-1}, with further spectra being acquired at 10 K intervals. The spectra acquired at temperatures of 50, 80, 110, 150, 180, 200, 220, and 225 K are shown in Fig. 3. An analysis of the spectral data presented in this figure reveals that IR spectra collected between 20 and 150 K are all fairly similar, indicating that no large-scale structural changes occurred within the ice over this temperature range and that the EtA likely remained largely amorphous.

At 180 K, however, changes to the spectrum became noticeable. In particular, absorption bands became sharper and narrower and were more easily distinguishable from neighbouring features. Such changes in the appearance of the spectra indicate a phase transition of the EtA ice from amorphous to crystalline. Indeed, further warming to 200 K caused the absorption bands to further sharpen and narrow, and absorption bands became even more easily distinguishable from their neighbours. This is especially true in the fingerprint region of the spectrum, where a series of distinct absorption features becomes apparent. Further warming to 220 K resulted in a reduction in the absorbance of the bands, indicating some degree of sublimation-induced mass-loss from the crystalline ice. At 225 K, no absorption features attributable to EtA can be observed in the acquired IR spectrum, indicating the complete sublimation of the ice. This process was also confirmed by complimentary gas-phase quadrupole mass spectrumetry (QMS) measurements, which initially recorded the presence of desorbed EtA at a temperature of about 203 K. Upon further increases in temperature, more extensive desorption was observed by the QMS, with significant and rapid sublimation of the ice occurring above 220 K. In agreement with IR results, complete sublimation of the ice was recorded at 225 K.

3.1.2.2 Isothermal desorption study Following the procedure described in Fuchs et al. (2009) (see their fig. 3), we performed an isothermal desorption experiment of pure EtA to estimate the value of the integrated strength constant of the absorption band at 1615 cm^{-1}
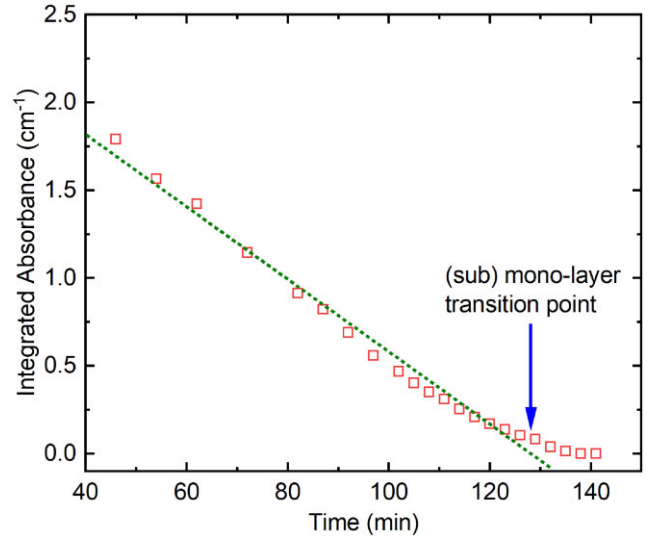

Figure 4. Integrated absorbance for the 1615 cm^{-1} absorption band as a function of time when an EtA ice deposited at 180 K is held at 210 K. The arrow indicates the subjectively selected transition point from the multilayer to the (sub)monolayer regime.

(NH$_2$ bending mode), indicated by the blue dashed rectangle in Fig 1. Pure EtA ice was deposited at 180 K and then rapidly heated to 210 K. Once the ice had equilibrated at this temperature, spectra were acquired at regular time intervals and the decline in the integrated absorbance of the absorption band at 1615 cm^{-1} due to the gradual sublimation of the ice was measured as a function of time (Fig. 4). By subjectively defining the point at which this decay trend changes, we have been able to estimate the integrated absorbance when the ice thickness shifts from the multilayer regime to the (sub)monolayer one, at which point the column density is on the order of 10^{15} molecules cm^{-2}. By following the method of Fuchs et al. (2009), we have approximated a value for the apparent absorption band strength of the EtA absorption band at 1615 cm^{-1}. We emphasize that this estimated value is set-up specific and there is a large uncertainty ($\pm$50 per cent) due to the fact that EtA may not adequately wet the ZnSe surface. Therefore, additional studies are required to adequately quantify the IR integrated band strength constants of solid EtA. Nevertheless, our derived value for this band strength constant is still meaningful in estimating the radiolytic destruction half-life of EtA.

3.2 Irradiation studies

Our work on the electron and He$^+$ ion irradiation of EtA-containing ices provides new insights into the radiolytic destruction of this species in astronomical environments. In this section, we present the results of irradiation experiments on EtA ices, pure and mixed with ASW at 20 K. IR and VUV spectroscopic data were respectively acquired at Atomki and ASTRID2, and are discussed separately.

3.2.1 Pure EtA ice

3.2.1.1 IR spectroscopy of 1 keV electron irradiated pure EtA ice A pure EtA ice having a thickness of 340 nm was deposited at 20 K and irradiated with 1 keV electrons. Changes in the IR spectral profile of the pure EtA ice as a result of electron irradiation were assessed by subtracting the spectrum collected directly after ice deposition from
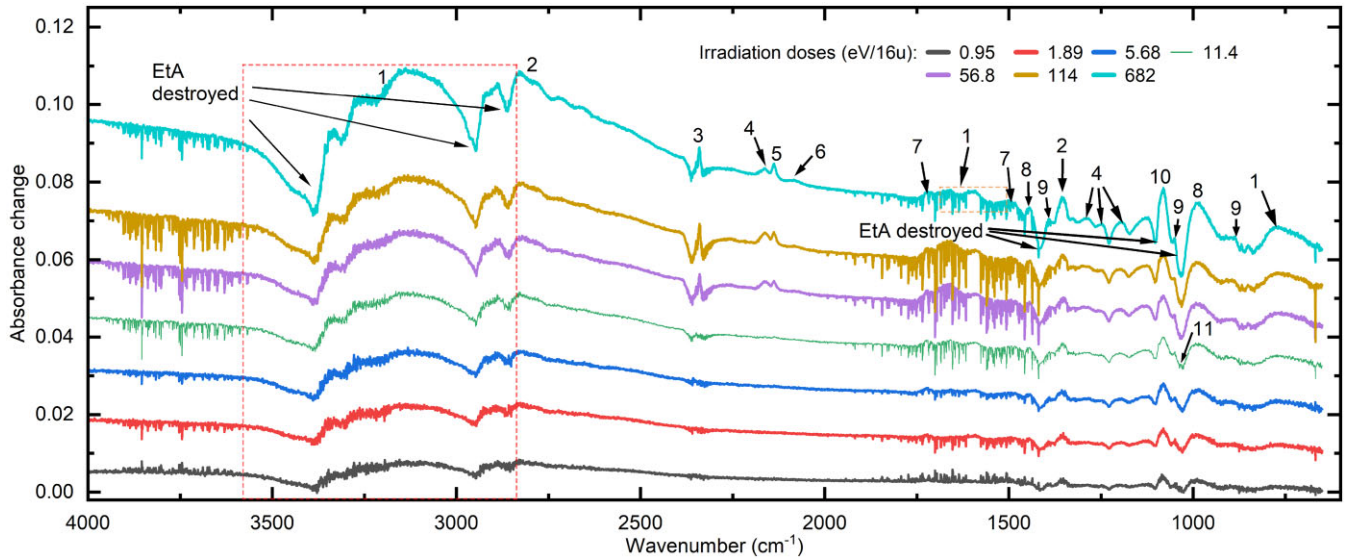
Figure 5. Change in the IR absorption spectrum of pure EtA ice during 1 keV electron irradiation. Spectra are vertically offset from one another with increasing irradiation dose for ease of viewing. The absorption bands corresponding to products are labelled using numbers, and the corresponding product species are listed in Table 3. Downward peaks including the ones in the dashed box indicate the destruction of EtA.

Table 3. Reaction products detected by means of IR spectroscopy during the 1 keV electron irradiation of pure EtA ice. Band numbers correspond to those shown in Fig. 5.

Band No.	1	2	3	4	5	6
Wavenumber (cm^{-1})	3200	2830	2340	2160	2140	2080
	1650	1350		1295		
	770			1250		
				1195		
Product	H_2O	H_2O_2	CO_2	OCN^-	CO	CN^-
References	*a*	*b*	*c, d*	*e*	*f*	*g, h*
Band No.	7	8	9	10	11	
Wavenumber (cm^{-1})	1720	1445	1390	1080	1030	
	1490	985	1050			
			885			
Product	HCHO	C_2H_4	C_2H_5OH	NH_3	CH_3OH	
References	*i*	*j*	*k*	*l*	*m, n*	

[a]Mifsud et al. (2022); [b]Hudson & Moore (2006); [c]Sandford & Allamandola (1990); [d]Isokoski, Poteet & Linnartz (2013); [e]Maté et al. (2012); [f]Gerakines et al. (1995); [g]Moore & Hudson (2003); [h]Noble et al. (2013); [i]Vinogradoff et al. (2013); [j]Molpeceres et al. (2017); [k]Terwisscha van Scheltinga et al. (2018); [l]Pilling et al. (2010); [m]Sandford & Allamandola (1993); [n]Ehrenfreund et al. (1999).

the spectra collected during irradiation, as shown in Fig. 5. The large downward bands are indicative of the radiolytic destruction of EtA; a detailed quantification of which will be presented later in this paper. The emergence of upward bands is associated with the growth of absorption features attributable to newly formed species (see Fig. 5 and Table 3). It is evident that H_2O is formed as a result of irradiation, along with other product molecules such as CO_2, CO, H_2CO, NH_3, and C_2H_4. We have ruled out the possibility that the observed H_2O is sourced from contamination of the ice by background gas within the chamber because we have quantitatively measured the background deposition of contaminants from the residual atmosphere in the ICA and have found that, in the worst case scenario, it does not exceed

a rate of 2×10^{15} molecules cm^{-2} per hour if a deposited ice is left undisturbed. Since our irradiation experiments were conducted on deposited ice samples with column densities on the order of 10^{17} molecules cm^{-2}, and since the irradiation of our ice should have reduced the deposition of background contaminants to at least some degree, we can safely assume that the amount of H_2O in our irradiated ice sourced from the deposition of background contaminants is negligible.

H_2O may be formed as a result of the radiolytic dissociation of EtA *via* a number of reaction steps. For instance, the dehydrogenation reactions shown in equations (4) and (5) could have resulted in the formation of H· in a similar fashion to that described by Hudson & Moore (2018) and Johnsen (1961) for the radiolysis of CH_3OH and C_2H_5OH.

$$NH_2CH_2CH_2OH \longrightarrow NH_2CH_2\dot{C}HOH + H\cdot \qquad (4)$$

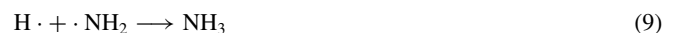$$NH_2CH_2CH_2OH \longrightarrow NH_2CH_2CH_2O\cdot + H\cdot \qquad (5)$$

The dissociation of EtA could also have conceivably yielded ·OH (see equation 6), which has also been observed during the irradiation of alcohols (Hudson & Moore 2018).

$$NH_2CH_2CH_2OH \longrightarrow NH_2CH_2\dot{C}H_2 + \cdot OH \qquad (6)$$
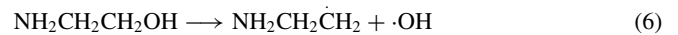
H_2O could then form as a result of the radical combination reaction between H· and ·OH (Ioppolo et al. 2008; Dulieu et al. 2010; Romanzin et al. 2011).

$$H\cdot + \cdot OH \longrightarrow H_2O \qquad (7)$$

NH_3 is likely to be formed through the cleavage of the C–N bond in the EtA molecule (Sladkova et al. 2014) followed by hydrogenation of the resultant ·NH_2 radical (Fedoseev et al. 2015a), as per equations (8) and (9).

$$NH_2CH_2CH_2OH \longrightarrow \cdot NH_2 + \cdot CH_2CH_2OH \qquad (8)$$

$$H\cdot + \cdot NH_2 \longrightarrow NH_3 \qquad (9)$$

The combination of ·CH_2CH_2OH from equation (8) and H· from equation (4) or (5) could result in the formation of C_2H_5OH, as per

equation (10).
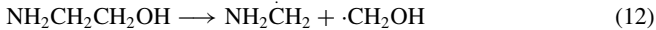
$$\cdot CH_2CH_2OH + H\cdot \longrightarrow C_2CH_5OH \qquad (10)$$
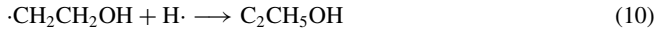
C_2H_4 could be formed through the dissociation of the EtA molecule *via* the simultaneous cleavage of its C−N and C−O bonds (see equation 11). Such a mechanism is qualitatively similar to that thought to be responsible for the formation of C_2H_4 during the radiolysis of C_2H_5OH (Freeman et al. 1974).

$$NH_2CH_2CH_2OH \longrightarrow \cdot NH_2 + C_2H_4 + \cdot OH \qquad (11)$$
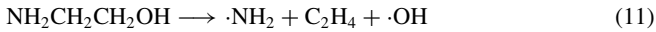
H_2CO could be formed through the cleavage of C–C bond in the EtA molecule, followed by dehydrogenation of the resultant $\cdot CH_2OH$ radical (see equations 12 and 13).

$$NH_2CH_2CH_2OH \longrightarrow NH_2\dot{C}H_2 + \cdot CH_2OH \qquad (12)$$

$$\cdot CH_2OH \longrightarrow H_2CO + H\cdot \qquad (13)$$

The irradiation-induced decomposition of H_2CO could also explain the formation of CO within our irradiated EtA ices (see equation 14).

$$H_2CO \longrightarrow CO + H_2 \qquad (14)$$

CH_3OH could be formed through two routes, either through the hydrogenation of CO formed through equation (14), or *via* the recombination of the $\cdot CH_2OH$ radical formed through equation (12) with H· formed through equations (4) and (5) (Fuchs et al. 2009).

$$CO + 4H\cdot \longrightarrow CH_3OH \qquad (15)$$

$$\cdot CH_2OH + H\cdot \longrightarrow CH_3OH \qquad (16)$$
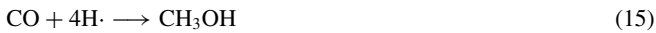
Finally, CO_2 could be formed through the reaction between CO and ·OH (Ioppolo et al. 2011).

$$CO + \cdot OH \longrightarrow CO_2 + H\cdot \qquad (17)$$

In order to evaluate the radiolytic destruction of the EtA ice when processed by 1 keV electrons, we have quantified the column density of EtA using equation (1) and have made use of our estimated integrated band strength constant for the EtA absorption band at $1615\,cm^{-1}$ (see section 3.1.2.2). It is important to note that the $1650\,cm^{-1}$ absorption band of H_2O partially overlaps with the EtA band of interest, and thus may lead to an underestimation of EtA radiolytic destruction. To compensate for this effect, we have used the H_2O absorption band at $770\,cm^{-1}$ to estimate the area of the band at $1650\,cm^{-1}$ based on the known ratio of the areas of these bands in a pure ASW ice at 20 K as measured in the same set-up under similar experimental conditions (Mifsud et al. 2022). The calculated area of the $1650\,cm^{-1}$ H_2O absorption band was then subtracted from the measured area of the $1615\,cm^{-1}$ band in irradiated EtA, thus refining our analysis.

The initial column density of EtA before irradiation was found to be 3.3×10^{17} molecules cm^{-2}. Fig. 6 shows that the EtA column density decreases with increasing radiation dose, and that the overall change after 1 h of irradiation is a loss of 9.76×10^{16} molecules cm^{-2}, corresponding to 29 per cent of the EtA having been destroyed. The irradiation dose D administered to the ice is calculated as follows:

$$D = F \times S, \qquad (18)$$

where F denotes the fluence, and S is the mass stopping power which, in the case of 1 keV electrons impacting pure EtA ice, is 5.88×10^{-15} eV $cm^2/16u$ (see Table 1). The irradiation dose D is in units of eV/16u to allow for the convenient characterization of
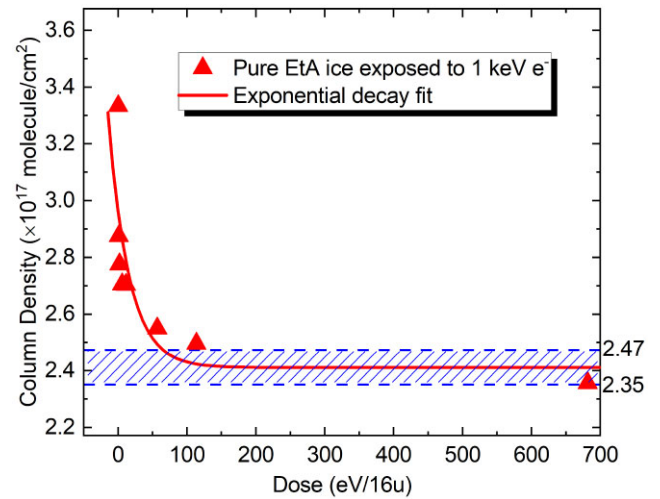

Figure 6. Calculated column density of pure EtA ice deposited at 20 K before and after 1 keV electron irradiation. The exponential decay function $N = 5.43\times10^{16}\exp(-D/30) + 2.4\times10^{17}$ has been fitted to the data. The shaded strip denotes the uncertainty range of the final amount due to lack of experimental data points between doses of 150 and 650 eV/16u.

chemical changes and for easier comparisons of experimental results (Strazzulla & Johnson 1991; Kobayashi et al. 2017). Fig. 6 also shows that most of the EtA survived irradiation due to the fact that the penetration depth of a 1 keV electron in pure EtA ice, which is calculated to be 45 nm (see Table 1) through a simulation performed using the CASINO software (Drouin et al. 2007), is much smaller than the thickness of the deposited EtA ice (340 nm). The profile of the data points in Fig. 6 suggested that the EtA column density followed an exponential decay trend during ice processing by 1 keV electrons, and the function $N = 5.43 \times 10^{16}\exp(-D/30) + 2.4 \times 10^{17}$ could be fitted to the data points. The half-life dose of pure EtA ice in our electron irradiation experiment is estimated as being 20.8 eV/16u from the fitted function. The exponential decay can also be described by the equation:

$$\frac{N_0 - N}{N_0} = \alpha \left(1 - e^{-\sigma F}\right), \qquad (19)$$

where N and N_0 respectively represent the column density after fluence F and the initial column density, α is the destruction fraction, and σ is the apparent destruction cross-section. By combining equations (18) and (19), and comparing with the fitted function, σ is calculated to be 2×10^{-16} cm^2.

3.2.1.2 VUV spectroscopy of 1 keV electron irradiated pure EtA ice
Complementary to the IR results, the VUV spectral data allowed us to qualitatively demonstrate the destruction of EtA during electron irradiation and the concomitant formation of new species. VUV spectra of pure EtA ice prior to and during its irradiation by 1 keV electrons are shown in Fig. 7. The lower wavelength limit of detection at $\lambda = 120$ nm is set by the transmission properties of the MgF_2 windows associated with the PAC set-up. Furthermore, it should be noted that the thickness of the pure EtA ice deposited in the VUV spectroscopic study was significantly less than that deposited during our IR spectroscopic study (40 *versus* 340 nm, respectively), due to the higher VUV absorption cross-sections of the ice which cause absorption features in the acquired spectra to saturate at much smaller thicknesses.
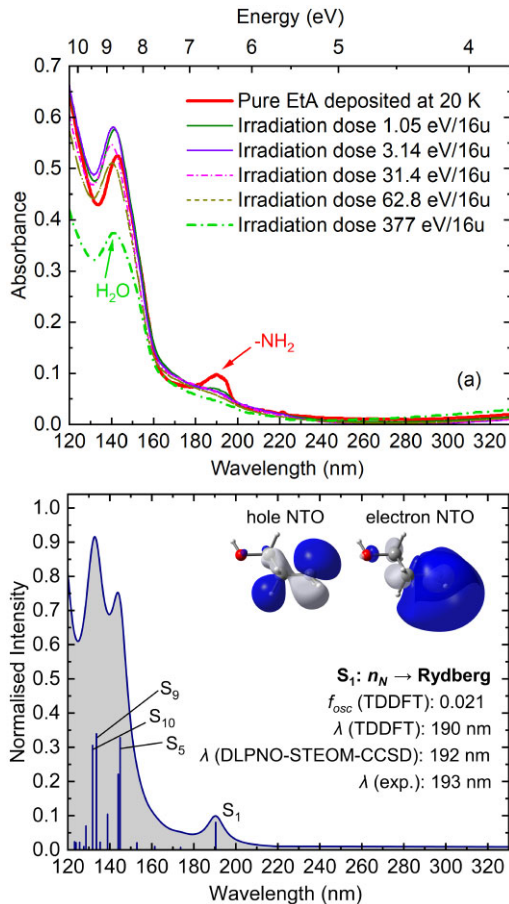
Figure 7. VUV spectra of deposited and electron irradiated EtA ice. (a) VUV (120–330 nm) spectra of pure EtA ice deposited at 20 K before and during 1 keV electron irradiation. The spectral ranges between 120–220 nm and 220–330 nm were respectively obtained with step sizes of 0.2 and 1 nm. (b) Simulated VUV spectrum of gaseous monomeric EtA from TDDFT calculations at the ωB97X-D3(BJ)/def2-QZVPP//PBE0-D3(BJ)/def2-TZVP level of theory. The inset orbitals are the hole and electron NTOs corresponding to the $S_0 \rightarrow S_1$ transition (isovalue: 0.03 au). The oscillator strength of this $n_N \rightarrow$ Rydberg electronic transition at the aforementioned level of theory and the calculated (TDDFT and DLPNO–STEOM–CCSD) and experimental wavelengths are shown for comparison. The S_5, S_9, and S_{10} states, which are the main contributors to the EtA portion of the experimental feature observed around 143 nm, are also highlighted.

The VUV spectrum of pure condensed EtA (Fig. 7) consists of an absorption feature that peaks at $\lambda < 120$ nm, a broad-band centred at $\lambda = 142$ nm, and a smaller band centred at $\lambda = 193$ nm. Since this is the first study of the VUV absorption spectroscopy of EtA ice, there are no references in the literature that may aid in assigning these bands to particular transitions. Therefore, we have performed TDDFT and DLPNO–STEOM–CCSD calculations in conjunction with the NTO analysis to aid in the interpretation of the acquired VUV spectra (see Section 2.3 for further details).

The band centred at $\lambda = 193$ nm is attributed to the NH$_2$ chromophore group of the amine moiety (see e.g. table 6.1 in Gokel 2004 and Goyal et al. 2008). The TDDFT calculations for the gaseous monomeric EtA are in perfect agreement with the experimental results in the condensed phase, with a band feature at $\lambda = 190$ nm. In these calculations, the monomeric geometry, taken directly from the crystal structure and optimized at the PBE0-D3(BJ)/def2-TZVP level, was considered. Similar results were obtained for other

EtA conformers. Inspection of the computed data (bottom panel in Fig. 7) reveals that this band is associated with the $S_0 \rightarrow S_1$ electronic transition. As the analysis of the frontier molecular orbitals points to a mixed contribution between the HOMO $\rightarrow$ LUMO (17 per cent) and the HOMO $\rightarrow$ LUMO + 1 (78 per cent) excitations (HOMO: highest occupied molecular orbital; LUMO: lowest unoccupied molecular orbital), the character of the $S_0 \rightarrow S_1$ electronic transition is analysed through NTO calculations. The results show that this transition involves electronic excitation from the nitrogen lone pair to a Rydberg-type orbital, and is therefore labelled as $n_N \rightarrow$ Rydberg. The calculated oscillator strength (f_{osc}) at the ωB97X-D3(BJ)/def2-QZVPP//PBE0-D3(BJ)/def2-TZVP level is 0.021. Similar results for both λ and f_{osc} are found for the monomeric EtA at the DLPNO–STEOM–CCSD level ($\lambda = 192$ nm; $f_{osc} = 0.019$) and for EtA oligomers at the TDDFT level ($\lambda = 181$–194 nm; $f_{osc} = 0.010 - 0.031$), all featuring the same type of excitation. Given the striking qualitative and quantitative similarity between the computed and measured data, and the growing number of condensed-phase systems where confined Rydberg transitions are observed (Ozaki & Tanabe 2016), we suggest that the 193 nm VUV spectral band of the pure EtA ice is indeed of the Rydberg type.

There is an intense feature centred at $\lambda = 142$ nm, and our TDDFT results show that the band is caused by different electronic states, the most intense being the $S_0 \rightarrow S_5$, $S_0 \rightarrow S_9$, and $S_0 \rightarrow S_{10}$ transitions. For the S_5 state, two NTO pairs have important contributions, one related to $n_N \rightarrow$ Rydberg (68 per cent) and the other to $n_O \rightarrow$ Rydberg (30 per cent). For the S_9 and S_{10} states, the excitation is solely dominated by an $n_O \rightarrow$ Rydberg character. Again, confined Rydberg-type transitions appear to be at play in the VUV spectrum of the EtA ice.

It is possible to observe that the NH$_2$ peak at $\lambda = 193$ nm decreases with increasing dose of electron irradiation, showing that the EtA is gradually destroyed by 1 keV electrons. By the end of the irradiation, the NH$_2$ peak disappears, indicating that almost all of the EtA had been destroyed by the electron bombardment. The major band (142 nm) still remains; however, it is shifted to lower wavelengths and its intensity is lower. The dashed–dotted green spectrum in Fig. 7, corresponding to the final electron irradiation dose of 377 eV/16u, is qualitatively similar to a VUV spectrum of a deposited mixed H$_2$O:EtA (20:1) ice as discussed in the next section (see Fig. 11). Therefore, we assign the band at 140 nm mostly to the transition $1b_1$:$\tilde{X}^1 A_1 \rightarrow 4a_1$:$\tilde{A}^1 B_1$ of H$_2$O ice rather than to just EtA (Cruz-Diaz et al. 2014). Finally, CASINO simulation results of the implantation of 1 keV electrons into pure EtA ice (see Table 1 and Drouin et al. 2007) indicate that the penetration depth of 1 keV electrons into pure EtA ice is 45 nm, which is comparable to the total thickness of the deposited ice in our VUV spectroscopy experiments. Therefore, we expect that the EtA ice layer is fully exposed to the incident 1 keV electrons and hence it is nearly all converted into other species. This is in agreement with the IR experiments shown in Section 3.2.1.1.

It is important to note that contamination due to deposition of background gases in the PAC during irradiation and VUV scanning of the EtA ice is negligible, as the spectral features of the EtA were not affected during the longer high-resolution VUV scans. This is in agreement with a previous work making use of the same experimental set-up and protocols (Dawes et al. 2017).

3.2.2 EtA in ASW

The irradiation of EtA in ASW (H$_2$O:EtA = 50:1) deposited at 20 K was investigated with a mixing ratio having been chosen so as to
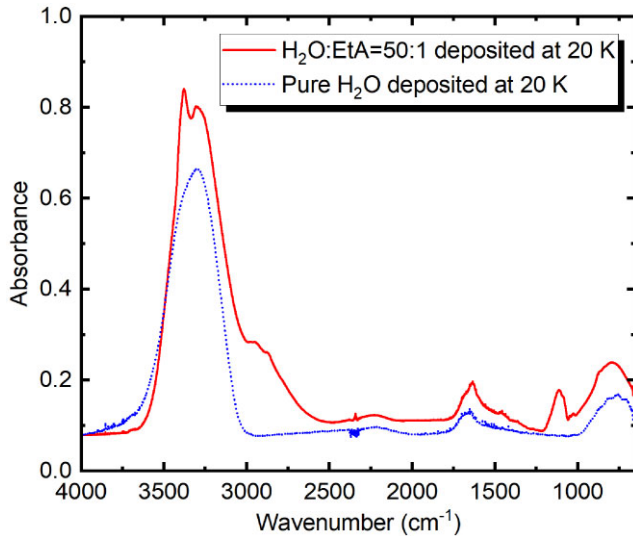
Figure 8. IR absorption spectrum of H_2O:EtA = 50:1 as deposited at 20 K, acquired with a spectral resolution of $0.5\,cm^{-1}$. The ice thickness is 1.40 μm. A spectrum of pure H_2O ice deposited at 20 K is also shown for comparison.

create a realistic analogue to ISM conditions, where H_2O is the main ice component in interstellar icy grain mantles and EtA is embedded in the porous ASW. The obtained IR spectrum from 4000–650 cm^{-1} for this ice analogue is shown in Fig. 8. It is worth noting that this IR spectrum is very similar to that of pure H_2O ice as indicated by the blue dotted spectrum, but also preserves many of the EtA absorption bands shown in Fig. 1. The electron irradiation of H_2O:EtA mixed ices were studied using IR and VUV spectroscopy and, to further simulate cosmic ray (CR) irradiation of interstellar ices, we also conducted the He$^+$ ion irradiation of the ice, and collected IR spectra to analyse the physical and chemical effects of ion irradiation.

3.2.2.1 IR spectroscopy of 1 keV electron irradiated H_2O:EtA mixed ice As was the case for the electron irradiation of pure EtA ice, we spectroscopically followed changes in the H_2O:EtA mixed ice induced by irradiation by subtracting the IR absorption spectrum acquired after deposition of the mixed ice from spectra subsequently acquired during irradiation (see Fig. 9). Here, downward bands are indicative of EtA or H_2O destruction as a result of the processing of the ice by impinging electrons, while the appearance of new absorption features is indicative of the formation of radiolytic product species (Fig. 9 and Table 4). Spectral changes of H_2O ice under electron irradiation are negligible as shown in the work of Ioppolo et al. (2021b), due to an equilibrium being established between the dissociation of H_2O molecules and the recombination of H atoms and OH radicals at 20 K. Similar to the irradiation of pure EtA ice, H_2O is formed as a result of the electron irradiation of the mixed ice, along with other products such as C_2H_5OH, CO_2, CO, and NH_3, that formed by reaction equations (7), (10), (17), (14), and (9), respectively.

To evaluate the radiolytic destruction of EtA in the ice mixture, we have analysed the variations in its column density as a function of the administered dose (Fig. 10) in a similar way to what was done for the pure EtA ice. A mass stopping power of 5.69×10^{-15} eV cm^2/16u for 1 keV electrons impacting the mixed ice was used to obtain the dose (see equation 18). The column density of EtA in the mixed ice prior to any irradiation was found to be 1.08×10^{17} molecules cm^{-2}, and our analysis has revealed that, after 1 h of electron irradiation, only 8 per cent of the EtA in the mixed ice had been destroyed. As shown

in Fig. 10, the column density evolution of the EtA ice as a function of increasing dose seemed to broadly follow an exponential decay. Using the fitted function to this exponential decay trend, we have been able to estimate the half-life dose $D_{1/2}$ as being 26.3 eV/16u. Moreover, using the fitted function together with equations (18) and (19), the apparent destruction cross-section σ is calculated to be 1.5×10^{-16} cm^2.

3.2.2.2 VUV spectroscopy of 1 keV electron irradiated H_2O:EtA mixed ice The irradiation of an H_2O:EtA (20:1) mixed ice at 20 K was also investigated using VUV spectroscopy at ASTRID2. The VUV spectra of the H_2O:EtA mixed ice prior to and during its irradiation by 1 keV electrons are shown in Fig. 11, which consists of an absorption feature that peaks at $\lambda < 120$ nm (only partially visible), and a broad band centred at $\lambda = 143$ nm. Due to the predominance of H_2O in the mixed ice, the acquired spectra are very similar to that of pure H_2O ice (Ioppolo et al. 2021b), and the NH_2 peak cannot be clearly seen. As the irradiation dose increases, there is a downward shift of the spectra, which provides complimentary qualitative evidence for the destruction of the EtA component of the ice.

3.2.2.3 IR spectroscopy of 1 MeV He$^+$ ion irradiated H_2O:EtA mixed ices A mixed H_2O:EtA ice (H_2O:EtA = 50:1) deposited at 20 K was irradiated using 1 MeV He$^+$ ions. The IR absorption spectrum of this ice is virtually identical to the one shown in Fig. 8 and, once again, proved to be similar to that of H_2O ice while retaining several absorption features of EtA. The thickness of the mixed ice processed by 1 MeV He$^+$ ions was estimated to be 1.40 μm using equation (2). The absorption spectra acquired during 1 MeV He$^+$ ion irradiation of the H_2O:EtA mixed ice allowed us to quantify the radiolytic destruction of EtA. Similar to the protocol followed during the electron irradiation experiments, we have subtracted the spectrum of the mixed ice acquired upon its deposition from subsequent spectra acquired during irradiation (Fig. 12). In this case, H_2O was observed to form as a result of He$^+$ ion irradiation. Additionally, greater quantities of CO_2 and CO were noted to form compared to the previous electron irradiation experiments, as indicated by the larger absorption features of these species in Fig. 12 compared to Figs 5 and 9. Other radiolysis products were also detected (Table 5), including NH_3, HNCO, OCN$^-$, CH_3CHO, and HCHO.

Changes in the molecular column density of EtA in the mixed ice as a result of its irradiation by 1 MeV He$^+$ ions (Fig. 13) were estimated in the same way as for the 1 keV electron irradiation experiments. The fluences and the mass stopping power of the incident 1 MeV He$^+$ ions (the latter being 7.143×10^{-14} eV cm^2/16u) were used to calculate the doses (as per equation 18). Prior to irradiation, an EtA column density of 7.99×10^{16} molecules cm^{-2} was present within the mixed ice. He$^+$ ion irradiation was found to be very effective at destroying the EtA in the ice, with 99.6 per cent of the EtA being destroyed after 1 h of irradiation (Fig. 13). By fitting the exponential decay curve $N = 7.46 \times 10^{16}$exp(D/15.54) + 7.79×10^{14} to the data points plotted in Fig. 13, we have been able to determine the half-life dose $D_{1/2}$ as being 10.8 ± 1.2 eV/16u. Almost no EtA is left in the mixed ice at the end of the 1 MeV He$^+$ ion irradiation. This greater destruction percentage of EtA compared to the analogous 1 keV electron irradiation experiment can be due to the greater penetration depths of the ions within the ice combined with their larger molecular destruction cross-sections. Indeed, a SRIM simulation (Ziegler, Ziegler & Biersack 2010) revealed that the penetration depth of 1 MeV He$^+$ ions into the mixed ice is up to 5.6 μm, far exceeding the ice thickness (1.40 μm) in this experiment (see Table 1). The apparent
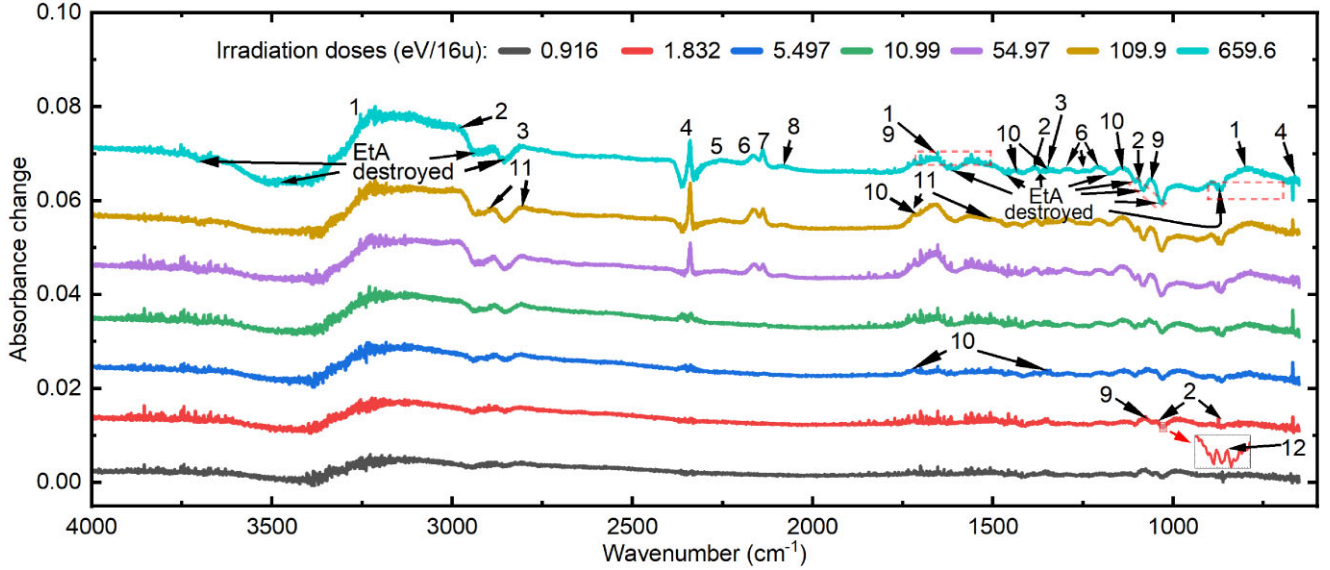
Figure 9. Change in the IR absorption spectrum of a mixed H_2O:EtA ice (H_2O:EtA = 50:1) during 1 keV electron irradiation. Spectra are vertically offset from one another for ease of viewing. The absorption bands corresponding to products are labelled and the nature of the product species are listed in Table 4.

Table 4. Reaction products detected during the 1 keV electron irradiation of H_2O:EtA = 50:1 mixed ice.

Band No.	1	2	3	4	5	6
Wavenumber (cm^{-1})	3250	2980	2810	2340	2260	2160
	1650	1390	1350	660		1295
	790	1045				1250
		875				1200
Product	H_2O	C_2H_5OH	H_2O_2	CO_2	HNCO	OCN^-
References	*a*	*b*	*c*	*d, e*	*f*	*g*
Band no.	7	8	9	10	11	12
Wavenumber (cm^{-1})	2140	2080	1650	1720	2890	1028
			1070	1440	2810	
				1350	1720	
				1130	1500	
Product	CO	CN^-	NH_3	CH_3CHO	HCHO	CH_3OH
References	*h*	*i, j*	*k*	*b*	*l*	*m, n*

[a]Mifsud et al. (2022); [b]Terwisscha van Scheltinga et al. (2018); [c]Hudson & Moore (2006); [d]Sandford & Allamandola (1990); [e]Isokoski et al. (2013); [f]Lowenthal, Khanna & Moore (2002); [g]Maté et al. (2012); [h]Gerakines et al. (1995); [i]Moore & Hudson (2003); [j]Noble et al. (2013); [k]Pilling et al. (2010); [l]Vinogradoff et al. (2013); [m]Sandford & Allamandola (1993); [n]Ehrenfreund et al. (1999).

destruction cross-section σ is calculated to be 4.6×10^{-15} cm^2, which is significantly larger than that calculated for the analogous electron irradiation experiment.

4 ASTROCHEMICAL IMPLICATIONS

Our IR and VUV spectroscopic analyses of the irradiated pure and mixed EtA ices have allowed us to demonstrate that, when subjected to electron irradiation (analogous to secondary electrons released within the ice) and He$^+$ ion irradiation (analogous to galactic CRs), EtA ice is destroyed and new radiolytic products are formed. The doses of electron and He$^+$ ion irradiation required to destroy a given amount of EtA can be used to estimate its survivability and stability in icy grain mantles in dense interstellar clouds and in icy outer Solar System bodies such as comets or Kuiper Belt Objects (KBOs). EtA
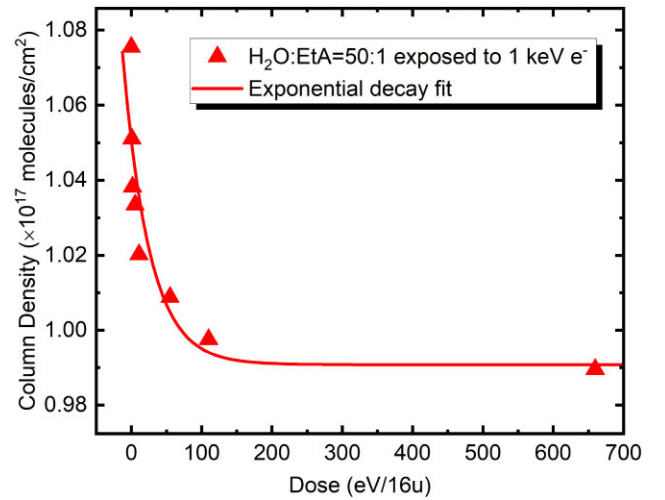

Figure 10. Calculated column density of EtA molecules in an H_2O:EtA = 50:1 ice mixture deposited at 20 K before and during 1 keV electron irradiation. The exponential decay function $N = 5.97 \times 10^{15}\exp(-D/38) + 9.91 \times 10^{16}$ has been fitted to the data.

in interstellar icy grain mantles and icy Solar System objects is likely diluted by other species, most notably H_2O, and is impinged upon by CRs which release a cascade of secondary electrons throughout the ice. Therefore, we use our derived half-life dose for a mixed H_2O:EtA ice in Subsection 3.2 together with literature values for irradiation dose rates in the dense ISM and KBOs to estimate the half-life of EtA in interstellar icy grain mantles and on the surface of icy Solar System objects. It is worthwhile noting that the mixed ice is an approximate representative for the ice in space where CO_2 and other species are also present. Our derived half-life dose of He$^+$ ion irradiation in the mixed ice (10.8 eV/16u) is the lowest among our three calculated values. The EtA half-life $T_{1/2}$ is calculated as follows:
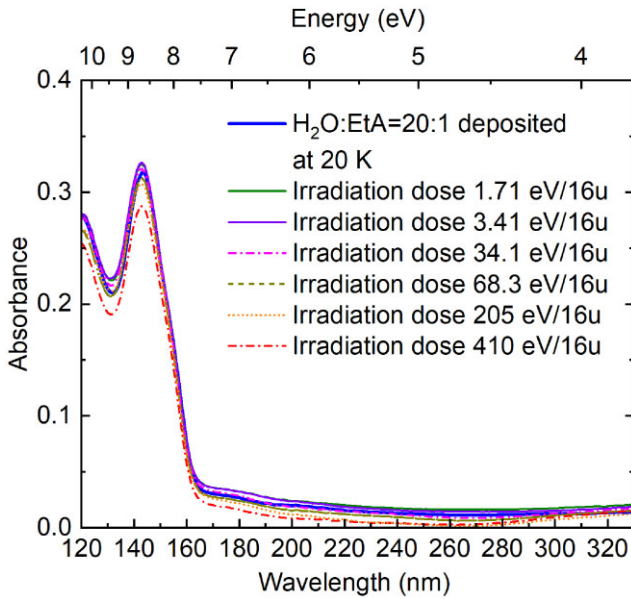
$$T_{1/2} = \frac{D_{1/2}}{R}, \tag{20}$$

Figure 11. VUV (120–330 nm) photoabsorption spectra of H_2O:EtA (20:1) mixed ice deposited at 20 K before and during 1 keV electron irradiation. Note that the indicated irradiation doses are upper limits of the delivered doses in this experiment. VUV spectra were obtained with a step size of 1 nm.
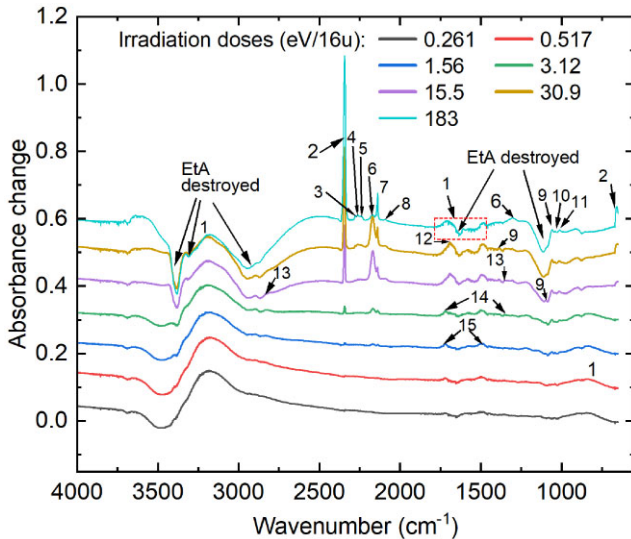

Figure 12. Change in the IR absorption spectrum of an H_2O:EtA = 50:1 mixed ice during 1 MeV He$^+$ irradiation. Spectra are vertically offset from one another for ease of viewing. The absorption bands corresponding to products are labelled and the nature of the product species are listed in Table 5.

where $D_{1/2}$ is the calculated half-life dose and R is the irradiation dose rate in the corresponding environments. We consider similar astronomical conditions to those considered by Maté et al. (2018), including dose rate, etc. It is important to note that the resultant half-life values are only meaningful in terms of their order of magnitude, as the literature values for CR doses themselves include many approximations (Maté et al. 2018).

The results of our half-life calculations are summarized in Table 6. The half-life of EtA ice in cold dense interstellar clouds is 3.6×10^7 yr which is on the same order of magnitude as the lifetime of interstellar

Table 5. Reaction products detected during the 1 MeV He$^+$ ion irradiation of an H_2O:EtA = 50:1 mixed ice.

Band No.	1	2	3	4	5	6	7	8
Wavenumber (cm^{-1})	3200	2340	2280	2260	2240	2170	2140	2090
	1700	660				1305		
	800							
Product	H_2O	CO_2	$^{13}CO_2$	HNCO	N_2O	OCN$^-$	CO	CN$^-$
References	a	b, c	d, e	f	d, e	g	h	d, e
Band no.	9	10	11	12	13	14	15	
Wavenumber (cm^{-1})	1390	1040	1015	1690	2820	1720	1720	
	1095				1350	1350	1500	
	1055							
Product	C_2H_5OH	O_3	CH_3OH	NH_2CHO	H_2O_2	CH_3CHO	HCHO	
References	i	j	k	l	m	j	n	

^{a}Mifsud et al. (2022); ^{b}Sandford & Allamandola (1990); ^{c}Isokoski et al. (2013); ^{d}Moore & Hudson (2003); ^{e}Noble et al. (2013); ^{f}Lowenthal et al. (2002); ^{g}Maté et al. (2012); ^{h}Gerakines et al. (1995); ^{i}Terwisscha van Scheltinga et al. (2018); ^{j}Hudson (2018); ^{k}Ehrenfreund et al. (1999); ^{l}Martín-Doménech, Öberg & Rajappan (2020); ^{m}Hudson & Moore (2006); ^{n}Vinogradoff et al. (2013).
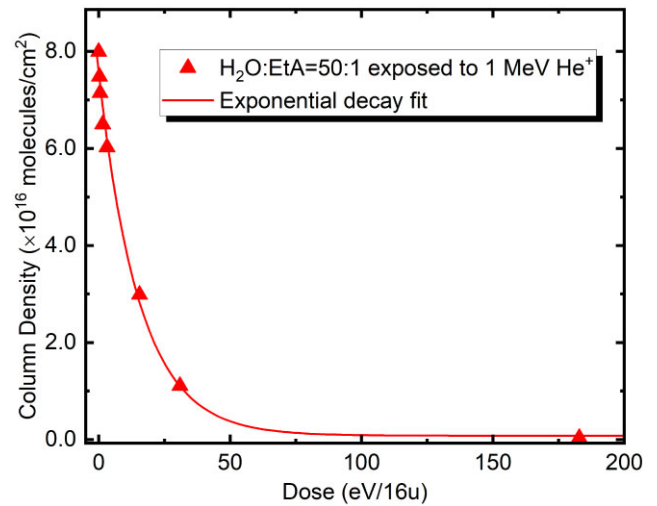

Figure 13. Calculated column density of EtA molecules in an H_2O:EtA = 50:1 mixture deposited at 20 K before and during 1 MeV He$^+$ ion irradiation. The exponential decay function $N = 7.46 \times 10^{16}\exp(D/15.54) + 7.79 \times 10^{14}$ is fitted to the data.

Table 6. Estimated half-life of EtA ice in interstellar icy grain manltes in cold dense clouds and in cometary or KBO ices.†.

Location of ice	Ice lifetime (yr)	Dose rate (eV· molecule^{-1} yr^{-1})	Half-life of EtA (yr)
Cold dense cloud	10^7	3×10^{-7} ^{a}	$(3.6 \pm 0.4) \times 10^7$
KBO (depth: $<1 \times 10^{-6}$ cm)	4.6×10^9	5.6×10^{-3} ^{b}	$(1.9 \pm 0.2) \times 10^3$
KBO (depth: 1×10^{-3} cm)	4.6×10^9	1.6×10^{-8} ^{c}	$(6.8 \pm 0.8) \times 10^8$

Notes. † We consider similar environments to Maté et al. (2018).
^{a}Moore, Hudson & Gerakines (2001).
^{b}Cooper et al. (2003). We consider a CR dose rate for surface ices of thickness $< 1 \times 10^{-6}$ cm.
^{c}Strazzulla et al. (2003). We consider a CR dose rate for ices at depths of 1×10^{-3} cm.

icy grain mantles, thus indicating that EtA should be very stable in such ices in the dense ISM. This stability, together with the continuous formation of COMs on icy grains, would suggest the abundant presence of EtA in the ISM. Conversely, a half-life of just 1900 yr is obtained for EtA ices on KBOs (thickness $< 1 \times 10^{-6}$ cm), suggesting a low survivability on the top surface of objects in the icy outer Solar System. However, if the EtA is embedded in the KBO surface at a depth of 1×10^{-3} cm, the half-life increases to

6.8×10^8 yr, demonstrating the radiolytic stability of EtA embedded within icy Solar System objects. Such a result helps to explain the presence of EtA on comet Wild-2 (Glavin et al. 2008), and aligns with the theory of an exogenous origin for life's biomolecules.

The recent detection of EtA toward the G+0.693−0.027 molecular cloud by gas-phase rotational transition spectroscopy in the millimetre-wave band (Rivilla et al. 2021) demonstrated the abundant presence of gas-phase EtA in the cold cloud. Based on the proposed formation routes for EtA on dust-grain surfaces (Charnley 2001; Ehrenfreund & Charnley 2001; Bernstein et al. 2002), Rivilla et al. (2021) inferred that EtA is ubiquitously present in the icy grain mantles in the cold cloud and that desorption from the ices has contributed to the gas-phase EtA detected. To confirm this, it is desirable to use IR observations to search for the presence of EtA in the ices in the cold, dense regions of the ISM. The IR spectroscopic data of EtA presented here will guide a potential future detection of EtA in the solid phase by means of space-borne observatories such as JWST.

The earlier detection of EtA in the Almahata Sitta meteorite (Glavin et al. 2010) also suggests the presence of EtA on Solar System objects. This is in agreement with our present analysis that demonstrates the stability of the EtA if it is embedded in KBO surfaces deeper than 1×10^{-3} cm. Therefore, searches for EtA in the Solar System should also be conducted by means of IR and UV observatories. The JWST is already in mission, and collected IR observational data for Solar System objects should be analysed and compared with our laboratory data to identify the potential presence of EtA. In addition, the recently launched JUICE mission may carry out both IR and UV observations and, upon its arrival at the Jovian System, will generate new data on the surface compositions of the Galilean satellites which may be compared against our laboratory data in the search for EtA (as well as other COMs) on those moons.

5 CONCLUSIONS

In this study, we have investigated the stability of EtA-containing ices in the icy ISM and Solar System through experiments that simulate the conditions in these astronomical environments. The experiments were primarily analysed using IR and VUV spectroscopic techniques. Heating studies of a pure EtA ice were performed, and IR spectra were collected at various temperatures. The results demonstrated a thermally induced solid phase change from an amorphous structure to a crystalline one at 180 K and full desorption at about 225 K. We have also analysed the stability of EtA-containing ices under electron and ion irradiation, and have calculated half-life doses for each type of irradiation. In particular, our experiments showed that He$^+$ ion irradiation is effective at destroying EtA due to its strong penetration capabilities and higher molecular destruction cross-sections.

The half-life doses calculated for electron irradiated pure and mixed EtA ices and for He$^+$ ion irradiated mixed EtA ice are 20.8 eV/16u, 26.3 eV/16u, and 10.8 eV/16u, respectively. It is evident that EtA mixed in H$_2$O ice is more stable against radiolytic decay than when it is in a pure form. Irradiation of the EtA ice produced a variety of product molecules, including H$_2$O, CO, CO$_2$, OCN$^-$, HNCO, NH$_3$, C$_2$H$_5$OH, and CH$_3$CHO, which were detected during the IR spectroscopy-based experiments conducted at Atomki. Using the ASTRID2 synchrotron, we have successfully obtained the VUV absorption spectra of EtA-containing ices and have made use of complementary TDDFT and DLPNO–STEOM–CCSD calculations to characterize the main absorption features of the pure EtA ice. The VUV spectra acquired during electron irradiation of the EtA-

containing ices also demonstrated the radiolytic destruction of EtA and formation of product molecules.

Moreover, we have applied our calculated half-life doses so as to gauge the survivability of EtA in interstellar icy grain mantles in cold dense clouds as well as in KBOs in the outer Solar System. Our analysis has shown that EtA diluted in H$_2$O ice in cold dense clouds has a half-life of 3.6×10^7 yr, indicating that EtA is stable in the dense ISM. If it is present on the surfaces of KBOs in the Solar System, it has a half-life of only 1900 yr. However, if EtA is embedded under the surface of the KBO at a depth of just 1×10^{-3} cm, then the half-life increases to 6.8×10^8 yr, suggesting that it is significantly more stable when embedded in icy Solar System objects. Finally, the IR and VUV spectroscopic characterizations of EtA presented here will guide its future detection in the ISM and in the Solar System by means of space-borne observatories such as JWST and JUICE.

DATA AVAILABILITY

Data will be made available to interested parties upon reasonable request of the corresponding authors.

REFERENCES

Adamo C., Barone V., 1999, J. Chem. Phys., 110, 6158
Altwegg K. et al., 2016, Sci. Adv., 43, e1600285

Bernstein M. P., Dworkin J. P., Sandford S. A., Cooper G. W., Allamandola L. J., 2002, Nature, 416, 401

Bertrand M., Van Der Gaast S., Vilas F., Hörz F., Haynes G., Chabin A., Brack A., Westall F., 2009, Astrobiol., 9, 943

Biri S. et al., 2021, Eur. Phys. J. Plus, 136, 247

Born M., Wolf E., 2013, Principles of optics: Electromagnetic theory of propagation, interference and diffraction of light. Cambridge Univ. Press, Cambridge

Brémond É., Savarese M., Su N. Q., Pérez-Jiménez Á. J., Xu X., Sancho-García J. C., Adamo C., 2016, J. Chem. Theory Comput., 12, 459

Budin I., Szostak J. W., 2011, Proc. Natl. Acad. Sci., 108, 5249

Chai J.-D., Head-Gordon M., 2008, J. Chem. Phys., 128, 084106

Charnley S. B., 2001, The Bridge Between the Big Bang and Biology. International Workshop, Stromboli, Italy, p. 139, https://books.google.co.uk/books?id = hJWyvwEACAAJ

Chizallet C., Costentin G., Che M., Delbecq F., Sautet P., 2007, J. Am. Chem. Soc., 129, 6442

Cooper G. W., Onwo W. M., Cronin J. R., 1992, Geochim. Cosmochim. Acta, 56, 4109

Cooper J. F., Christian E. R., Richardson J. D., Wang C., 2003, Earth Moon Planets, 92, 261

Craciunescu L. et al., 2022, J. Phys. Chem. Lett., 13, 3726

Craciunescu L. et al., 2023, J. Chem. Theory Comput., 19, 9369

Cruz-Diaz G. A., Muñoz Caro G. M., Chen Y.-J., Yih T.-S., 2014, A&A, 562, A119

Dawes A., Pascual N., Hoffmann S. V., Jones N. C., Mason N. J., 2017, Phys. Chem. Chem. Phys. (Incorporating Faraday Transactions), 19, 27544

Drouin D., Couture A. R., Joly D., Tastet X., Aimez V., Gauvin R., 2007, Scanning: J. Scanning Microsc., 29, 92

Dulieu F., Amiaud L., Congiu E., Fillion J. H., Matar E., Momeni A., Pirronello V., Lemaire J. L., 2010, A&A, 512, A30

Eden S., Limão-Vieira P., Hoffmann S., Mason N., 2006, Chem. Phys., 323, 313

Ehrenfreund P., Charnley S. B., 2001, in Proceedings of the First European Workshop Exo-/astro-biology, p. 35

Ehrenfreund P. et al., 1999, A&A, 350, 240

Ernzerhof M., Scuseria G. E., 1999, J. Chem. Phys., 110, 5029

Fedoseev G., Ioppolo S., Zhao D., Lamberts T., Linnartz H., 2015a, MNRAS, 446, 439

Fedoseev G., Cuppen H. M., Ioppolo S., Lamberts T., Linnartz H., 2015b, MNRAS, 448, 1288

Fedoseev G., Qasim D., Chuang K.-J., Ioppolo S., Lamberts T., van Dishoeck E. F., Linnartz H., 2022, ApJ, 924, 110

Ferrero S., Ceccarelli C., Ugliengo P., Sodupe M., Rimola A., 2023, ApJ, 951, 150

Freeman G. R. et al., 1974, Radiation chemistry of ethanol: A review of data on yields, reaction rate parameters, and spectral properties of transients. US Department of Commerce, National Bureau of Standards., Washington, D. C., USA

Frisch M. J. et al., 2016, Gaussian 16, Revision C.01. Gaussian, Inc., Wallingford CT

Fuchs G. W., Cuppen H. M., Ioppolo S., Romanzin C., Bisschop S. E., Andersson S., van Dishoeck E. F., Linnartz H., 2009, A&A, 505, 629

Gerakines P. A., Schutte W. A., Greenberg J. M., van Dishoeck E. F., 1995, A&A, 296, 810

Ghormley J. A., Hochanadel C. J., 1971, Science, 171, 62

Glavin D. P., Dworkin J. P., Sandford S. A., 2008, Meteorit. Planet. Sci., 43, 399

Glavin D. P. et al., 2010, Meteorit. Planet. Sci., 45, 1695

Gokel G., 2004, Dean's Handbook of Organic Chemistry. McGraw-Hill, New York, https://books.google.co.uk/books?id = -x6aDAEACAAJ

Goodman A. M., 1978, Appl. Opt., 17, 2779

Goyal D. K., Pribil G. K., Woollam J. A., Subramanian A., 2008, Mater. Sci. Eng. B., 149, 26

Grimme S., Antony J., Ehrlich S., Krieg H., 2010, J. Chem. Phys., 132, 154104

Grimme S., Ehrlich S., Goerigk L., 2011, J. Comput. Chem., 32, 1456

Herczku P. et al., 2021, Rev. Sci. Instrum., 92, 084501

Hudson R. L., 2018, ApJ, 867, 160

Hudson R. L., Moore M. H., 2006, Astrobiol., 6, 483

Hudson R. L., Moore M. H., 2018, ApJ, 857, 89

Ioppolo S., Cuppen H. M., Romanzin C., van Dishoeck E. F., Linnartz H., 2008, ApJ, 686, 1474

Ioppolo S., van Boheemen Y., Cuppen H. M., van Dishoeck E. F., Linnartz H., 2011, MNRAS, 413, 2281

Ioppolo S., Kanuchova Z., James R. L. et al., 2020, A&A, 641, A154

Ioppolo S. et al., 2021a, Nat. Astron., 5, 197

Ioppolo S., Kanuchova Z., James R. L. et al., 2021b, A&A, 646, A172

Isokoski K., Poteet C. A., Linnartz H., 2013, A&A, 555, A85

Johnsen R. H., 1961, J. Phys. Chem., 65, 2144

Johnson R. D. III, 2022, NIST Stand. Ref. Database Number 101. NIST, Gaithersburg

Kalout H., Boubegtiten-Fezoua Z., Maurel F., Hellwig P., Ferlay S., 2022, Phys. Chem. Chem. Phys., 24, 15103

Kandratsenka A., Schwarzer D., Vöhringer P., 2008, J. Chem. Phys., 128, 244510

Katsyuba S. A., Spicher S., Gerasimova T. P., Grimme S., 2020, J. Phys. Chem. B, 124, 6664

Knop S., Lindner J., Vöhringer P., 2011, Z. Phys. Chem., 225, 913

Kobayashi K. et al., 2017, Astrobiology, 17, 786

Kozuch S., Martin J. M. L., 2013, J. Comput. Chem., 34, 2327

Krasnokutski S. A., 2021, Low Temp. Phys., 47, 199

Krueger P. J., Mettee H. D., 1965, Can. J. Chem., 43, 2970

Lowenthal M., Khanna R., Moore M. H., 2002, Spectrochim. Acta Part A Mol. Biomol. Spectrosc., 58, 73

Martin R. L., 2003, J. Chem. Phys., 118, 4775

Martín-Doménech R., Öberg K. I., Rajappan M., 2020, ApJ, 894, 98

Maté B., Herrero V. J., Rodríguez-Lazcano Y., Fernández-Torre D., Moreno M. A., Gómez P. C., Escribano R., 2012, ApJ, 759, 90

Maté B., Molpeceres G., Tanarro I., Peláez R. J., Guillemin J. C., Cernicharo J., Herrero V. J., 2018, ApJ, 861, 61

McCaffrey V. P., Zellner N. E. B., Waun C. M., Bennett E. R., Earl E. K., 2014, Orig. Life Evol. Biosph., 44, 29

McGuire B. A., 2022, ApJS, 259, 30

Mifsud D. V. et al., 2021, Eur. Phys. J. D, 75, 182

Mifsud D. V. et al., 2022, Eur. Phys. J. D, 76, 87

Molpeceres G., Rivilla V. M., 2022, A&A, 665, A27

Molpeceres G. et al., 2017, MNRAS, 466, 1894

Molpeceres G., Kästner J., Fedoseev G., Qasim D., Schömig R., Linnartz H., Lamberts T., 2021, J. Phys. Chem. Letters, 12, 10854

Monnard P.-A., Deamer D. W., 2011, The Minimal Cell, Springer. Berlin, p. 123–151

Moore M. H., Hudson R. L., 2003, Icarus, 161, 486

Moore M., Hudson R., Gerakines P., 2001, Spectrochim. Acta Part A Mol. Biomol. Spectrosc., 57, 843

Neese F., 2022, WIREs Comput. Mol. Sci., 12, 1

Noble J. A., Theule P., Borget F., Danger G., Chomat M., Duvernay F., Mispelaer F., Chiavassa T., 2013, MNRAS, 428, 3262

Nooijen M., Bartlett R. J., 1997, J. Chem. Phys., 107, 6812

Novak A., 1974, in Large Molecules. Springer, Berlin, Heidelberg, p. 177

Oró J., Sherwood E., Eichberg J., Epps D., 1978, Light Transducing Membranes. Academic Press, New York, USA, p. 1

Ozaki Y., Tanabe I., 2016, Analyst, 141, 3962

Palmer M. H. et al., 2015, J. Chem. Phys., 142, 134302

Pilling S., Seperuelo Duarte E., da Silveira E. F., Balanzat E., Rothard H., Domaracka A., Boduch P., 2010, A&A, 509, A87

Pizzarello S., Shock E., 2010, Cold Spring Harbor Perspect. Biol., 2, a002105

Potapov A., Krasnokutski S. A., Jäger C., Henning T., 2021, ApJ, 920, 111

Radom L., Lathan W. A., Hehre W. J., Pople J. A., 1973, J. Am. Chem. Soc., 95, 693

Rajta I. et al., 2018, Nucl. Instrum. Methods Phys. Res A, 880, 125

Rao M., Eichberg J., Oró J., 1987, J. Mol. Evol., 25, 1

Reitmeier R. E., Sivertz V., Tartar H. V., 1940, J. Am. Chem. Soc., 62, 1943

Riplinger C., Neese F., 2013, J. Chem. Phys., 138, 034106

Riplinger C., Sandhoefer B., Hansen A., Neese F., 2013, J. Chem. Phys., 139, 134101

Rivilla V. M. et al., 2021, Proc. Natl. Acad. Sci., 118, e2101314118

Romanini M. et al., 2019, Cryst. Growth Des., 19, 6360

Romanzin C., Ioppolo S., Cuppen H. M., van Dishoeck E. F., Linnartz H., 2011, J. Chem. Phys., 134, 084504

Sandford S., Allamandola L., 1990, Astrophysical Journal, Part 1 (ISSN 0004-637X), vol. 355, May 20, 1990, p. 357-372., 355, 357

Sandford S. A., Allamandola L. J., 1993, ApJ, 417, 815

Sephton M. A., 2002, Nat. Prod. Rep., 19, 292

Sharma J., Champagne P. A., 2022, J. Comput. Chem., 43, 2131

Silva C. F., Duarte M. L. T., Fausto R., 1999, J. Mol. Struct., 482-483, 591

Sladkova A. A., Lisovskaya A. G., Sosnovskaya A. A., Edimecheva I. P., Shadyro O. I., 2014, Rad. Phys. Chem., 96, 229

Strazzulla G., Johnson R. E., 1991, Irradiation Effects on Comets and Cometary Debris. Springer, Netherlands, Dordrecht, p. 243

Strazzulla G., Cooper J. F., Christian E. R., Johnson R. E., 2003, Comptes Rendus Phys., 4, 791

Stuart B. H., 2004, Spectral Analysis. John Wiley & Sons, Ltd, Chichester, p. 45

Suzuki T., Majumdar L., Ohishi M., Saito M., Hirota T., Wakelam V., 2018, ApJ, 863, 51

Terwisscha van Scheltinga J., Ligterink N. F. W., Boogert A. C. A., van Dishoeck E. F., Linnartz H., 2018, A&A, 611, A35

Tseng C.-L., Chen Y.-K., Wang S.-H., Peng Z.-W., Lin J.-L., 2010, J. Phys. Chem. C, 114, 11835

Vinogradoff V., Duvernay F., Danger G., Theulé P., Borget F., Chiavassa T., 2013, A&A, 549, A40

Vorobyov I., Yappert M. C., DuPré D. B., 2002, J. Phys. Chem. A, 106, 668

Weigend F., Ahlrichs R., 2005, Phys. Chem. Chem. Phys., 7, 3297

Yuan X. et al., 2018, Phys. Chem. Chem. Phys., 20, 20779

Zhang Q., Chen T., Ma L., Tang Z., Yu L., 2021, Chem. Phys. Lett., 767, 138350

Zhu C., Turner A. M., Abplanalp M. J., Kaiser R. I., Webb B., Siuzdak G., Fortenberry R. C., 2020, ApJ, 899, L3

Ziegler J. F., Ziegler M. D., Biersack J. P., 2010, Nucl. Instrum. Methods Phys. Res. B, 268, 1818

SUPPORTING INFORMATION

Supplementary data are available at *MNRAS* online.

Please note: Oxford University Press is not responsible for the content or functionality of any supporting materials supplied by the authors. Any queries (other than missing material) should be directed to the corresponding author for the article.

[1] *School of Electronic Engineering and Computer Science, Queen Mary University of London, London E1 4NS, UK*

[2] *Institute of Materials Science of Madrid (ICMM), CSIC, c/ Sor Juana Inés de la Cruz 3, E-28049 Madrid, Spain*

[3] *HUN-REN Institute for Nuclear Research (Atomki), Debrecen H 4026, Hungary*

[4] *Astronomical Institute, Slovak Academy of Sciences, Tatranská Lomnica SK 059 60, Slovakia*

[5] *Centre for Astrophysics and Planetary Science, School of Physics and Astronomy, University of Kent, Canterbury CT2 7NH, UK*

[6] *Laboratory for Astrophysics, Leiden Observatory, Leiden University, PO box 9513, 2300 RA Leiden, the Netherlands*

[7] *Centre for Interstellar Catalysis, Department of Physics and Astronomy, Aarhus University, DK 8000 Aarhus, Denmark*

[8] *Institute of Chemical Sciences, School of Engineering and Physical Sciences, Heriot-Watt University, Edinburgh EH14 4AS, UK*

[9] *ISA, Department of Physics and Astronomy, Aarhus University, DK 8000 Aarhus, Denmark*

[10] *School of Physical Sciences, The Open University, Milton Keynes MK7 6AA, UK*

[11] *Atomic Molecular and Optical Physics Division, Physical Research Laboratory, Ahmedabad 380009, India*

[12] *School of Chemistry and Forensic Science, University of Kent, Canterbury CT2 7NH, UK*

This paper has been typeset from a TEX/LATEX file prepared by the author.